Structural, optical and electrical properties of $WO_x(N_y)$ films deposited by reactive dual magnetron sputtering

Sodky H. Mohamed[1,2] and André Anders[1]

[1]Lawrence Berkeley National Laboratory, University of California, 1 Cyclotron Road, California 94720, USA

[2]Physics Department, Faculty of Science, South Valley University, 82524 Sohag, Egypt

Abstract

Thin films of tungsten oxynitrides were prepared by dual magnetron sputtering of tungsten using argon/oxygen/nitrogen gas mixtures with various nitrogen/oxygen ratios. The presence of even relatively small amounts of oxygen led to close-to-stoichiometric WO_3, with little incorporation of nitrogen, therefore the films were labeled as $WO_x(N_y)$. Oxygen had a great effect not only on the composition but on the structure of $WO_x(N_y)$ films, as shown by Rutherford backscattering and x-ray diffraction, respectively. Significant incorporation of nitrogen occurred only when the nitrogen partial pressure exceeded 89% of the total reactive gas pressure. Sharp changes in the stoichiometry, deposition rate, room temperature resistivity, electrical activation energy and optical band gap were observed when the nitrogen/oxygen ratio was high. The deposition rate increased from 0.31 to 0.89 nm/s,

the room temperature resistivity decreased from 1.65×10^{8} to 1.82×10^{-2} Ωcm, the electrical activation energy decreased from 0.97 to 0.067 eV, and the optical band gap decreased from 3.19 to 2.94 eV upon nitrogen incorporation into the films. $WO_x(N_y)$ films were highly transparent as long as the nitrogen incorporation was low, and were brownish (absorbing) and partially reflecting as nitrogen incorporation became significant.

Keywords: Dual magnetron sputtering; tungsten oxynitride thin films; structural, electrical, optical properties

1. Introduction

Tungsten trioxide (WO_3) has a high capability to reversibly change its optical properties by insertion or extraction of small ions (e.g. H, Li) and charge-compensating electrons [1]. This makes it suitable for use in a variety of applications such as smart windows, nonemissive display devices, variable reflectance mirrors, and variable emissivity surfaces [1, 2]. WO_3 is also used as an active layer in gas sensors since it has the ability to decrease its high resistance when gasses are adsorbed [3, 4]. Tungsten nitrides, on the other hand, are characterized by high melting point, high hardness, chemical inertness and good thermal stability [5]. For these reasons, they are used for diffusion barriers in

microelectronics [6, 7] and electrodes in semiconductor devices [8]. Therefore, a combination of these materials as tungsten oxynitride, WO_xN_y, promises the possibility to tune the structural, optical and electrical properties in a wide range as desired for various applications.

In the last decade, transition metal oxynitride thin films have received considerable interest due to their interesting properties. The introduction of nitrogen into the oxide lattice or oxygen into the nitride lattice resulted in modifications of the film properties. For example, the substitution of oxygen by nitrogen in the TiO_2 [9], ZrO_2 [10] or Ta_2O_5 [11] lattice increased the index of refraction. This is because the metal-nitrogen bonds tend to be less polar than the corresponding metal-oxygen bonds, which leads to a higher polarizability for the metal nitrides [12] and a decrease of the optical band gap. The color is particularly changed by the more covalent bond character introduced by nitrogen upon oxygen replacement in *A*-WO_x, where *A* is a rare earth element [13], or by nitrogen replacement in ZrN [14]. The introduction of oxygen into the tungsten nitride lattice relieves residual stress [15]. Transition metal oxynitrides can be used in numerous applications; for example, CrO_xN_y can be used for temperature–dependence resistors in thermal radiation detectors [16], TiO_xN_y can serve as diffusion barriers in silicon-on-sapphire integrated circuits [17] and as decorative coatings [18], HfO_xN_y can be used as gate material in metal-oxide-semiconductor

devices [19], and rare earth-WO_xN_y materials are promising as novel pigments [13].

Reactive dual magnetron sputtering is a well established process for the deposition of compound films. The term "dual" refers to the presence of two magnetrons whose targets serve as alternating cathode and anode. The material is sputtered when the target is the cathode (negative) and serves as the electron collector when it is the anode (positive). The reasons for using such system are (i) to deal with the "disappearing anode" effect, i.e. the coating of the anode with an insulating film, and (ii) to reduce or prevent arcing on the target. The alternation (switching) of polarity is typically done in the mid-frequency (10-200 kHz) range [20]. In our system, two reactive gases (oxygen, nitrogen) are used which leads to some non-trivial modification of the reactive deposition process [21].

Compared to transition metal oxides and nitrides, the transition metal oxynitrides are poorly explored. In particular, very little has been done on WO_xN_y. The main purpose of this work was to study the compositional, structural, electrical and optical properties of WO_xN_y films as a function of the reactive gas partial pressure ratio. Because oxygen was much more readily incorporated in the films than nitrogen, the set of samples we report on was labeled $WO_x(N_y)$.

2. Experimental details

$WO_x(N_y)$ films were prepared on microscopic glass slides and Si (100) substrates by reactive dual magnetron sputtering of metallic tungsten targets in an argon, oxygen and nitrogen gas mixture. The magnetrons were "linear" sources with rectangular targets of 17.5 cm length and 5 cm width. The oxygen-nitrogen gas mixture was feed through a plasma source (of the Constricted Plasma Source type [22]) operated at 1500 W. The plasma source was positioned in the center between the two magnetrons, which were 15 cm apart. The purpose of the plasma source was to enhance the activation of the reactive gases by providing a higher density of ions, excited atoms, and molecules. For this work, no further studies were done to quantify the effects of the plasma source, as opposed to using reactive gas only.

The substrate were ultrasonically cleaned in acetone and dried with a flow of pure nitrogen before mounting on the substrate holder. The substrate holder was kept at ground potential.

Sputtering was started with the substrates at room temperature. An infrared temperature sensor was moving with the substrate recording the temperature of the substrate's backside surface.

The substrate was constantly moved, back and forth, in front of the two magnetrons and the plasma source; the closest distance between substrate and targets was 5 cm.

The cryogenically pumped vacuum system had a base pressure of 1.3×10^{-4} Pa at

full pumping speed of 1500 l/s for air. To accommodate the relatively high pressure during sputtering, the pumping speed was throttled to about 25% of its maximum, resulting in a throttled base pressure of about 1.3×10^{-3} Pa. The total pressure during deposition was kept constant at 0.53 Pa as monitored by a Baratron® capacitance manometer. The total pressure was kept constant by adjusting the Ar flow while systematically varying the O_2 and N_2 partial pressures. Details about the O_2, N_2, and Ar flow rates are listed in Table 1.

A differentially pumped gas monitor (PPM 100 by SRS) was used to measure the partial pressures during deposition. This gas monitor was pre-calibrated via the readings of the Baratron.

To prepare WO_xN_y films, we started with an O_2 partial pressure (P_{O_2}) of 0.364 Pa at 50 sccm O_2 flow. At this oxygen partial pressure, the W targets operated in the "poisoned" mode (oxide layer was present). Next, the O_2 flow was partially replaced by N_2 flow. The N_2 partial pressure (P_{N_2}) increased from 1.11×10^{-2} to 5.23×10^{-1} Pa (corresponding to a flow rate of 0 to 50 sccm N_2) while the O_2 partial pressure decreased from 3.64×10^{-1} to 3.68×10^{-4} Pa (by reducing the O_2 flow from 50 to 0 sccm). In this way, oxynitride films of different compositions could be obtained. In the remainder of this paper, we will use Γ, which we define as the nitrogen partial pressure normalized by the partial pressures of both reactive gases, $\Gamma \equiv P_{N_2} / \left(P_{N_2} + P_{O_2} \right)$.

The sputtering power was provided by a SPIK2000A pulser (Melec GmbH/NanoMaster) fed by a Pinnacle® Dual DC power supply (Advanced Energy Inc.). The frequency was set to 50 kHz and the power of 1.5 kW was equally shared between the two magnetrons.

Glass slide substrates were used for x-ray diffraction (XRD) because of the amorphous structure, and for measurements of the optical properties because of the high transparency in the visible range. Si(100) substrates were used for film thickness measurements (Dektak IIA profilometer) and compositional analysis (Rutherford back scattering, RBS). The profilometer had experimental error of about ± 10 nm in determining the film thickness. RBS was carried out using a 1.95 MeV $^{4}He^{+}$ ion beam generated by a 2.5 MeV Van de Graaff electrostatic accelerator. The samples were mounted on a two-axis goniometer. The backscattered particles were collected by a silicon surface barrier detector positioned at 165° with respect to the incident beam. The samples were tilted at various angles (from 5-50°) to optimize depth resolution. The compositions of the samples were obtained by best fitting the RBS spectra using the standard RUMP analysis software [23]. The experimental error on the amounts of oxygen and nitrogen was approximately ±15%.

The crystallographic structure of the films was determined by x-ray diffraction using a Siemens D-500 diffractometer with a Cu tube operated at 40 kV and 30 mA. The

measurements were carried out using Cu K_α radiation with a Ni filter to remove the Cu K_β reflections.

The spectral transmittance (T) and reflectance (R) were measured at normal incidence using a Perkin-Elmer Lambda-19 spectrophotometer in the wavelength range λ=300-2500 nm. The angle for the reflectance measurement was 8 degrees off normal.

The glass slides had pre-sputtered silver contacts of well defined length and distance, allowing us to record the sheet resistance of the films using a two-terminal configuration. The electrical contacts pads were made by masked silver sputtering, similar to previous work [24]. After film deposition, the samples were placed in an oven and temperature dependent measurements of the dc conductivity were carried out in the range 303 – 503 K. During measurements, the samples were in air and without illumination. A constant voltage of 10 V was applied to the contact pads and the current through the film was measured using a Keithley 410 picoamp-meter. With the thickness as per Table 1 we could readily determine the resistivity.

3. Results and Discussions

3.1 Film composition and structure

Figure 1 shows the deposition rate of $WO_x(N_y)$ deposited at different partial pressure ratios. The deposition rate was nearly constant up to $\Gamma = 0.693$. A steep increase in deposition rate was observed for $\Gamma > 0.693$. This behavior may be understood by considering the conditions on the target surfaces: a compound layer was formed on the presence of a reactive gas. As long as oxygen was the only reactive gas, the compound layer was tungsten oxide. When nitrogen is introduced and the oxygen partial pressure is reduced, the oxide is partially substituted by a nitride. The fact that the deposition rate was approximately constant up to $\Gamma = 0.693$ indicated that the character of the compound layer had not much changed. For $\Gamma > 0.693$, the compound layer changed; we may conclude that nitrogen reacted with tungsten, at least partially replacing the oxide, leading to a reduction of surface charging and an increase of the sputter yield, among other effects. In a first approximation, one can better understand the effects using dynamic Monte Carlo simulation. Using the code T-DYN 4.0 by Biersack [25] and assuming 500 eV Ar^+ as projectiles, we found that the partial sputter yield for tungsten is slightly greater from N-rich material compared to O-rich material. The results are summarized in Table 2. The main effect, however, is that the reactive gas component is preferentially sputtered, and therefore the target surface becomes more metallic as the sputtering evolves. A surface with a greater metal content has an even greater sputter yield, which confirms to well known fact that

sputtering tends to operated in either metallic or poisoned mode. Although dynamic Monte Carlo simulations using the universal ZBL (Ziegler-Biersack-Littmark) potential have been proven to be surprisingly accurate, we point out that these results should be see more qualitatively then quantitatively due to the binary collision approximation and other underlying assumptions.

It is interesting to compare the experimental reactive deposition rates with the deposition rate of 3 nm/s for the pure metal mode obtained (i.e., sputtering with Ar gas only). Therefore, going back to our reactive system, the rate of 0.9 nm/s at high Γ indicates that a nitride layer was present on the target and that the system has not yet reached the metal mode.

The composition of $WO_x(N_y)$ films prepared at different Γ was measured by RBS. The experimental data could be well fitted and interpreted by RUMP simulations. The results are shown in Fig. 2 and Table 1. One can see that there was no significant nitrogen incorporation for nitrogen partial pressures up to $\Gamma = 0.840$. For $\Gamma > 0.840$, compounds of $WO_x(N_y)$ were formed. The composition of these films did not linearly dependent on Γ because W possesses a stronger affinity to oxygen than to nitrogen. The oxygen content of the films was always higher than the corresponding nitrogen content in the process gas. Thermodynamically, the formation of tungsten oxide is energetically strongly favored over the formation of tungsten nitride or a NO

layer: the heat of formation for WO_3 and WO_2 is -842.9 kJ/mol and -589.7 kJ/mol, respectively, which greatly exceeds the values for W_2N (-22 kJ/mol), WN (-15 kJ/mol) [26], and NO (91.3 kJ/mol) [27, 28]. Furthermore, from Fig. 2 one can see that even if some of the nitrogen atoms were adsorbed and "buried" by the arriving W atoms [9], they did not become incorporated for $\Gamma \leq 0.840$. This may be ascribed to a nitrogen desorption mechanism which is induced by oxygen reacting with the W-[NO]-W structure, where nitrogen is released from the network as an interstitial NO molecule, leaving a peroxy linkage in its place [29].

Figure 3 shows typical XRD patterns of $WO_x(N_y)$ films deposited at different Γ. The pure WO_3 film was amorphous (Fig. 3a); the broad peak centered at about $2\theta = 25°$ stems from the glass substrate. This was expected since WO_3 crystallizes only when the temperature exceeds 200°C [30], while the maximum temperature that the film could reach via the plasma process heating was about 170°C. Starting at room temperature, the sample's temperature increased approximately linearly with time, indicating that the heating power was not balanced by any of the heat loss mechanisms (conduction, radiation).

No change in the amorphous structure was observed as long as Γ did not exceed 0.992. i.e., we observed a crystalline structure only when a large amount of nitrogen was incorporated. The observed peaks for the films prepared at $\Gamma = 0.999$ can be associated with cubic WN [31]. It is interesting to note that the transition from amorphous to

crystalline structures does not exactly coincide with the start of nitrogen incorporation. Nitrogen incorporation was observed for $\Gamma > 0.889$, whereas crystalline phases were observed for $\Gamma = 0.999$. The formation of a specific crystalline phase is affected by the composition, the temperature, and the possibility of competitive growth of different phases. In the WO_xN_y system, it is also possible that WO_xN_y crystallizes in a single phase and that a nanocomposite multiphase structure may form [32] containing substoichiometric WO_x and WN_y as well as stoichiometric WO_3 and WN crystallites. It is further noticed that the stoichiometry for $\Gamma = 0.999$ films was $WN_{1.8}$, as determined by RBS, which contains more nitrogen than the stoichiometric WN. The excess nitrogen atoms are believed to exist at the grain boundaries between tungsten nitride crystallites [33].

3.2 Electrical Properties

Tungsten oxide, WO_3, is a wide band n-type semiconductor that is very insulating as long as the material is stoichiometric, whereas tungsten nitride has metallic character. Figure 4 shows the room temperature resistivity of $WO_x(N_y)$ films as a function of Γ. The resistivity of WO_3 films deposited at $\Gamma = 0.029$ was 1.65×10^8 Ωcm. This value is higher than the reported values (10^3-10^7 Ωcm) for r. f. sputtered WO_3 films [34] It is known that the conductivity of WO_3 films depends on the O_2/Ar ratio during the sputtering process [34].

According to Gillet *et al.* [35] the conductivity of WO_3 is governed by the non-stoichiometry which originates from oxygen vacancies. The high resistivity value stayed almost constant upon increasing Γ to 0.840. For $\Gamma > 0.840$, the resistivity decreased sharply to reach a value of 1.8×10^{-2} Ωcm at $\Gamma = 0.999$. This can be explained by the increase of the metallic bond contribution and the formation of nitrogen doped WO_3, as was proposed for zirconium oxynitride [14].

The electrical conductivity σ can be written as an exponential function of temperature, *T*,

$$\sigma(T) = \sigma_0 \exp(-E_A / k_B T), \qquad (1)$$

where E_A is the activation energy for electrical conduction, which is a function of the electronic energy levels of the chemically interacting atoms in the amorphous materials and hence of the emerging band gap, σ_0 is the pre-exponential factor including the charge carrier mobility and density of states, and k_B is the Boltzmann constant. The activation energy can be derived from an Arrhenius plot of such dependence (Fig. 5). The linear fit was taken only for the data points at which there is an indication for thermal activation process (i.e., ignoring the first few points), and the results for various films obtained at different Γ are compiled in Fig. 6. The activation energy and pre-exponential factor show sharp decrease upon nitrogen incorporation in the WO_3 films. Electronic conduction takes

place in the extended state above the mobility edge or by hopping in localized states that can be distinguished on the basis of the pre-exponential factor, σ_0. It was suggested by Mott and Davis [36] (p. 382) that the pre-exponential factor for conduction in localized states should be two or three orders smaller in magnitude than for conduction in the extended states and should become still smaller for conduction in the localized states near the Fermi level. If the value of the pre-exponential factor is in the range of 10^3–10^4 $\Omega^{-1}cm^{-1}$, the conduction is mostly in extended states. A smaller value of the pre-exponential factor would indicate a wide range of localized states and conduction by hopping [37] In our $WO_x(N_y)$ thin films, the calculated σ_0 values for the films prepared for $\Gamma < 0.889$ were in the range of 10^6 $\Omega^{-1}cm^{-1}$. This suggested that the conduction in these films was due to thermally assisted charge carrier movement in the extended states. The calculated σ_0 values for the films prepared at $\Gamma > 0.889$ are in the range of 10^1 - 10^2 $\Omega^{-1}cm^{-1}$. Therefore, the possibility of extended state conduction is decreased and localized states conduction in the band tail is most likely. The incorporation of nitrogen in the film modified the microstructure and induced states near the conduction band thereby increasing the carrier density.

3.3 Optical Properties

Figure 7 shows the optical transmittance spectra of $WO_x(N_y)$ films deposited at

various Γ. There was no significant change in transmittance upon increasing Γ up to 0.840. For $\Gamma > 0.840$, the absorption edge shifted towards greater wavelengths (see insert Fig.7). The films changed from colorless for $\Gamma \leq 0.840$ to light brownish for $0.840 < \Gamma < 0.993$. For $\Gamma > 0.993$, metallic WO_xN_y films with higher absorption were obtained.

Using the measured spectral transmittance and reflectance, and the film thickness, *d*, the absorption coefficient α was calculated according to

$$\alpha = \frac{1}{d} \ln\left(\frac{1-R}{T}\right). \quad (2)$$

The optical band gap, E_g, was determined using the following formula

$$\alpha h\nu = \beta(h\nu - E_g)^n \quad (3)$$

where β is a constant and *n* is equal to 2 or ½ for allowed indirect or direct transitions, respectively. The E_g values are extracted from the $(\alpha h\nu)^{1/2}$ vs. $h\nu$ plot, indicating an indirect band gap for all of the examined $WO_x(N_y)$ films. The band gap E_g shows a sharp decrease upon nitrogen incorporation in WO_3 film (Fig. 8). Band gap narrowing by nitrogen incorporation has been previously observed in different transition metal oxynitrides [9, 10, 12, 15, 16, 38].

Different approaches have been adopted to interpret this effect. Investigations by Futsuhara *et al.* [39] provided an interpretation based on the change in ionicity upon nitrogen

incorporation. The optical band gap was related to the difference in ionicity between metal-O and metal-N bonds. Ionicity in a single bond increases with the difference in values of electronegativity between two elements forming the bond. The electronegativity of oxygen (3.5) is greater than that of nitrogen (3.0), which indicates that the metal-O bond involves a larger charge transfer than the metal-N bond. Thus, assuming that metal-O and metal-N bonds coexist in the films, the shift of the band gap can be attributed to the decrease in ionicity and hence to an increase of polarizability as the nitrogen content is increased.

A different approach based on density of states calculations was introduced by Asahi *et al.* [40]. They concluded that the substitutional doping of N into TiO_2 leads to the band gap narrowing by mixing N 2*p* states with O 2*p* states. This second approach is supported by simulations by Choi *et al.* [41] who investigated the HfO_xN_y system. They demonstrated that the N 2*p* states extends toward the conduction band as the N concentration increases and the ionic character of Hf-N bonding is less pronounced, resulting in a reduction of the band gap. Asahi's result was challenged by Di Valentin *et al.* [42] using density functional theory calculations. They showed that the N-doping into TiO_2 is accompanied by the presence of well localized N 2p states above the O 2p valence band states. Interrelation of such energy levels in the band gap reduces the band gap and increases the visible light absorption through a charge transfer between a dopant and a conduction or valence band.

4. Conclusions

Tungsten oxynitride films were prepared by reactive dual magnetron sputtering on glass and Si(100) substrates at different oxygen and nitrogen partial pressures. Nitrogen is only incorporated in the films at relatively high partial pressures of nitrogen. As nitrogen is incorporated, interesting modifications of the stoichiometric, structural, electrical and optical properties occur due to new electronic states which reduce the band gap and resistivity, and change the mechanism of conduction. With increasing nitrogen content, the films changes from highly transparent to brownish semi-reflecting. These oxynitride films may be used for decorative coatings and they are also interesting for electronic devices such as sensors in thermal radiation detectors.

Acknowledgements

The authors are grateful for technical support by Sakon Sansongsiri and Michael Dickinson. One of us (S. H. M.) would like to express his sincere gratitude to the Fulbright Commission for a fellowship to carry out this research work at Lawrence Berkeley National Laboratory. This work was also supported by the Assistant Secretary for Energy Efficiency and Renewable Energy, Office of Building Technology, of the U.S. Department of Energy under Contract No. DE-AC02-05CH11231.

References

[1] C. G. Granqvist, *Handbook of Inorganic Electrochromic Materials*. Amsterdam: Elsevier, 1995.

[2] C. G. Granqvist, E. Avendano, and A. Azens, *Thin Solid Films* 442 (2003) 201.

[3] M. Stankova, X. Vilanova, E. Llobet, J. Calderer, C. Bittencourt, J. J. Pireaux, and X. Correig, *Sensors and Actuators B* 105 (2005) 271.

[4] J. Guérin, K. Aguir, M. Bendahan, and C. Lambert-Mauriat, *Sensors and Actuators B* 104 (2005) 289.

[5] L. E. Toth, *Transition Metal Carbides and Nitrides*. New York: Academic Press, 1971.

[6] B. H. Lee and K. Yong, *J. Vac. Sci. Technol. B* 22 (2004) 2375.

[7] J. S. Becker and R. G. Gordon, *Appl. Phys. Lett.* 82 (2003) 2239.

[8] B.-L. Park, M.-B. Lee, K.-J. Moon, H.-D. Lee, H.-K. Kang, and M.-Y. Lee, "Comparison of PECVD-WN_x and CVD-TiN films for the upper electrode of Ta_2O_5 capacitors," IEEE 1998 Int. Interconnect Technol. Conf., San Francisco, CA, 1998, 96-98.

[9] S. H. Mohamed, O. Kappertz, J. M. Ngaruiya, T. Niemeier, R. Drese, R. Detemple, M. M. Wakkad, and M. Wuttig, *physica status solidi (a)* 201 (2004) 90.

[10] J. M. Ngaruiya, O. Kappertz, C. Liesch, P. Müller, R. Dronskowski, and M. Wuttig, *physica status solidi (a)* 201 (2004) 967.

[11] S. Venkataraj, D. Severin, S. H. Mohamed, J. Ngaruiya, O. Kappertz, and M. Wuttig, *Thin Solid Films* 502 (2006) 228.

[12] M. Ohring, *Materials Science of Thin Films. Deposition and Structure*, 2nd ed. San Diego: Academic Press, 2002.

[13] N. Diot, O. Larcher, R. Marchand, J. Y. Kempf, and P. Macaudiere, *J. Alloys and Compounds* 323-324 (2001) 45.

[14] P. Carvalho, F. Vaz, L. Rebouta, L. Cunha, C. J. Tavares, C. Moura, E. Alves, A. Cavaleiro, P. Goudeau, E. L. Bourhis, J. P. Riviere, J. F. Pierson, and O. Banakh, *J. Appl. Phys.* 98 (2005) 023715.

[15] Y. G. Shen and Y. W. Mai, *J. Mater. Res.* 15 (2000) 2437.

[16] R. Mientus, R. Grötschel, and K. Ellmer, *Surf. Coat. Technol.* 200 (2005) 341.

[17] N. Kumar, M. G. Fissel, K. Pourrezaei, B. Lee, and E. C. Douglas, *Thin Solid Films* 153 (1987) 287.

[18] F. Vaz, P. Cerqueira, L. Rebouta, S. M. C. Nascimento, E. Alves, P. Goudeau, J. P. Riviere, K. Pischow, and J. de Rijk, *Thin Solid Films* 447-448 (2004) 449.

[19] C.-L. Cheng, K.-S. Chang-Liao, and T.-K. Wang, *Solid-State Electronics* 50 (2006) 103.

[20] E. V. Barnat and T.-M. Lu, *Pulsed Sputtering and Pulsed Bias Sputtering*. Boston: Kluwer Academic Publishers, 2003.

[21] W. D. Sproul, D. J. Christie, and D. C. Carter, *Thin Solid Films* 491 (2005) 1.

[22] A. Anders, R. A. MacGill, and M. Rubin, *IEEE Trans. Plasma Sci.* 27 (1999) 82.

[23] L. R. Doolittle, *Nucl. Instrum. Meth. Phys. Res. B* 9 (1985) 344.

[24] E. Byon, T. H. Oates, and A. Anders, *Appl. Phys. Lett.* 82 (2003) 1634.

[25] J. P. Biersack, *Nucl. Instrum. Meth. Phys. Res. B* 59/60 (1991) 21.

[26] F. R. de Boer, R. Boom, W. C. M. Mattens, A. R. Miedema, and A. K. Niessen, *Cohesion of Metals*. Amsterdam: North Holland, 1988.

[27] D. R. Lide, (Ed.), *Handbook of Chemistry and Physics, 81st Edition*. Boca Raton, New York: CRC Press, 2000.

[28] M. Uekubo, T. Oku, K. Nii, M. Murakami, K. Takahiro, S. Yamaguchi, T. Nakano, and T. Ohta, *Thin Solid Films* 286 (1996) 170.

[29] W. Orellana, A. J. R. da Silva, and A. Fazzio, *Phys. Rev. B* 72 (2005) 205316.

[30] E. Washizu, A. Yamamoto, Y. Abe, M. Kawamura, and K. Sasaki, *Solid State Ionics* 165 (2003) 175.

[31] *Powder Diffraction Files, Joint Committee on Powder Diffraction Standards, JCPDS, Card 65-2898.*, 1998.

[32] O. Banakh, T. Heulin, P. E. Schmid, H. L. Dreo, I. Tkalcec, F. Levy, and P. A. Steinmann, *J. Vac. Sci. Technol. A* 24 (2006) 328.

[33] M. H. Tsai, S. C. Sun, H. T. Chiu, and S. H. Chuang, *Applied Physics Letters* 68 (1996) 1412.

[34] S. C. Moulzolf, S.-a. Ding, and R. J. Lad, *Sensors and Actuators B* 77 (2001) 375.

[35] M. Gillet, C. Lemire, E. Gillet, and K. Aguir, *Surface Science* 532-535 (2003) 519.

[36] N. F. Mott and E. A. Davis, *Electronics Processes in Non-Crystalline Materials*. Oxford: Clarendon, 1979.

[37] S. A. Khan, M. Zulfequar, Z. H. Khan, M. Ilyas, and M. Husain, *Optical Materials* 20 (2002) 189.

[38] Y. C. Hong, C. U. Bang, D. H. Shin, and H. S. Uhm, *Chem. Phys. Lett.* 413 (2005) 454.

[39] M. Futsuhara, K. Yoshioka, and O. Takai, *Thin Solid Films* 317 (1998) 322.

[40] R. Asahi, T. Morikawa, T. Ohwaki, K. Aoki, and Y. Taga, *Science* 293 (2001) 269.

[41] J. Choi, R. Puthenkovilakam, and J. P. Chang, *Ext. Abstr. Electrochem. Soc.* 502 (2006) 522.

[42] C. Di Valentin, G. Pacchioni, and A. Selloni, *Phys. Rev. B* 70 (2004) 085116.

Figure Captions

Fig. 1 Deposition rate of $WO_x(N_y)$ as a function of the normalized nitrogen partial pressure, $\Gamma = P_{N_2} / \left(P_{N_2} + P_{O_2} \right)$.

Fig. 2 Oxygen and nitrogen concentrations in $WO_x(N_y)$ films as a function of $\Gamma = P_{N_2} / \left(P_{N_2} + P_{O_2} \right)$.

Fig. 3 X-ray diffraction patterns of $WO_x(N_y)$ deposited at different Γ.

Fig. 4 Room temperature resistivity of $WO_x(N_y)$ films as a function of Γ.

Fig. 5 Arrhenius plot of the conductivity, ln(σ) versus 1000/T, σ in Ω cm, for $WO_x(N_y)$ films prepared at various $\Gamma = P_{N_2} / \left(P_{N_2} + P_{O_2} \right)$.

Fig. 6 Electrical activation energy (a), and the pre-exponential factor (b), calculated from the slopes and the intercepts of Fig. 5, respectively, as a function of $\Gamma = P_{N_2} / \left(P_{N_2} + P_{O_2} \right)$.

Fig. 7 Transmittance of $WO_x(N_y)$ films prepared at various $\Gamma = P_{N_2} / \left(P_{N_2} + P_{O_2} \right)$. The thicknesses of the films were in the range 420-600 nm.

Fig.8 Optical band gap of $WO_x(N_y)$ films as a function of $\Gamma = P_{N_2} / \left(P_{N_2} + P_{O_2} \right)$.

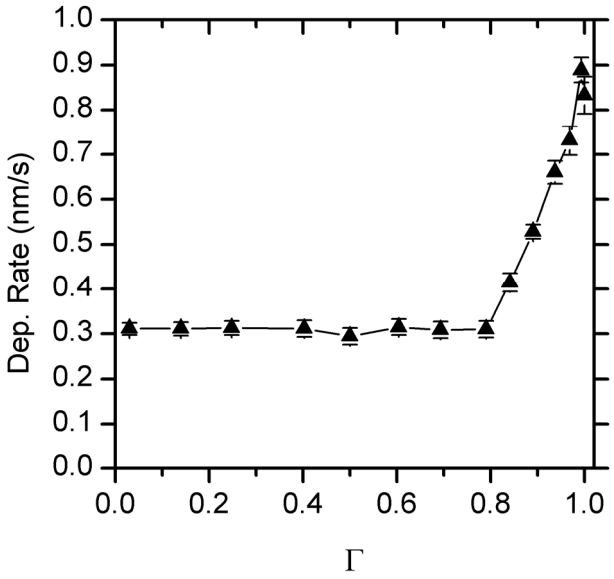

Fig. 1

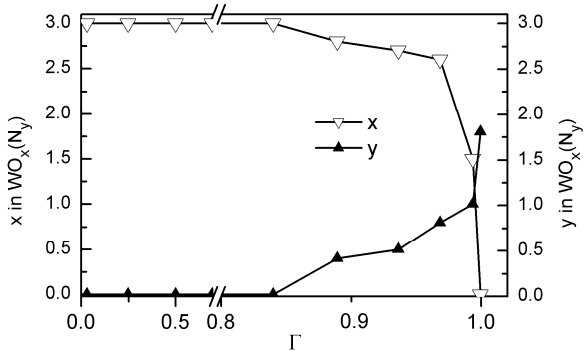

Fig. 2

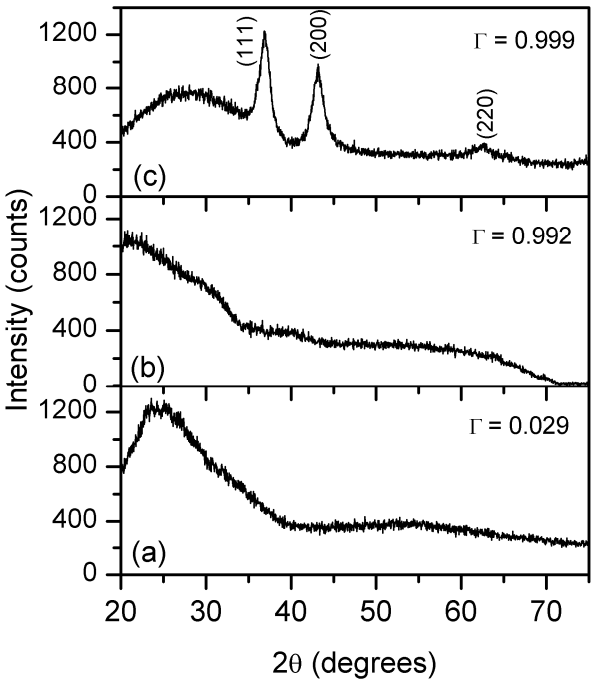
(111)
(200)
(220)
Γ = 0.999
Γ = 0.992
Γ = 0.029
(c)
(b)
(a)
Intensity (counts)
2θ (degrees)
0
400
800
1200
20
30
40
50
60
70

Fig. 3

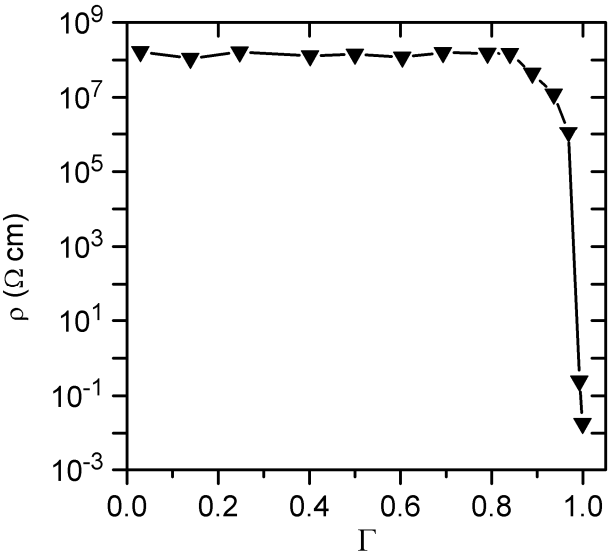

Fig. 4

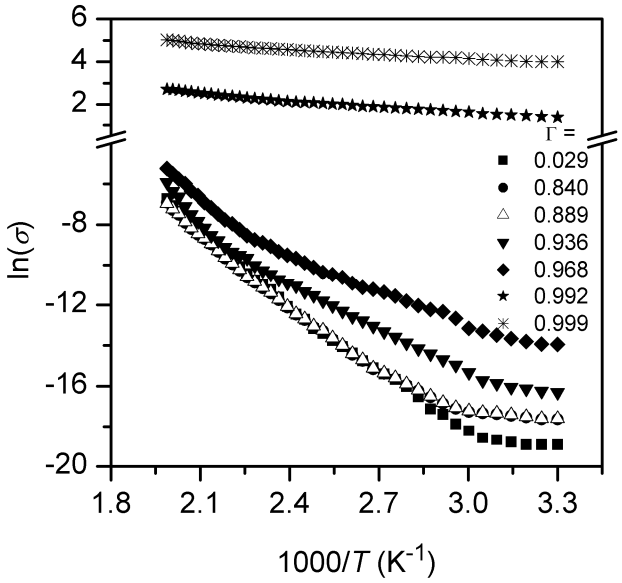
6
4
2
-8
-12
-16
-20
ln(σ)
1.8
2.1
2.4
2.7
3.0
3.3
1000/T (K-1)
Γ =
0.029
0.840
0.889
0.936
0.968
0.992
0.999

Fig. 5

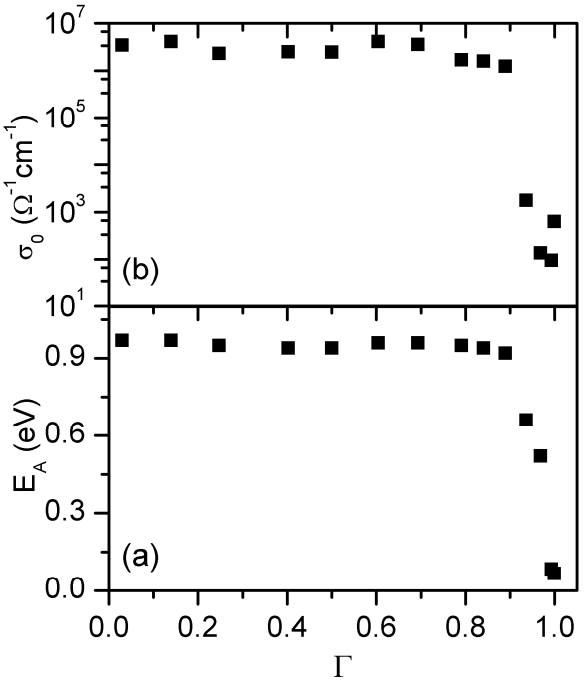
10^7
10^5
10^3
10^1
σ_0 (Ω^{-1}cm^{-1})
(b)
0.9
0.6
0.3
0.0
E_A (eV)
(a)
0.0
0.2
0.4
0.6
0.8
1.0
Γ

Fig. 6

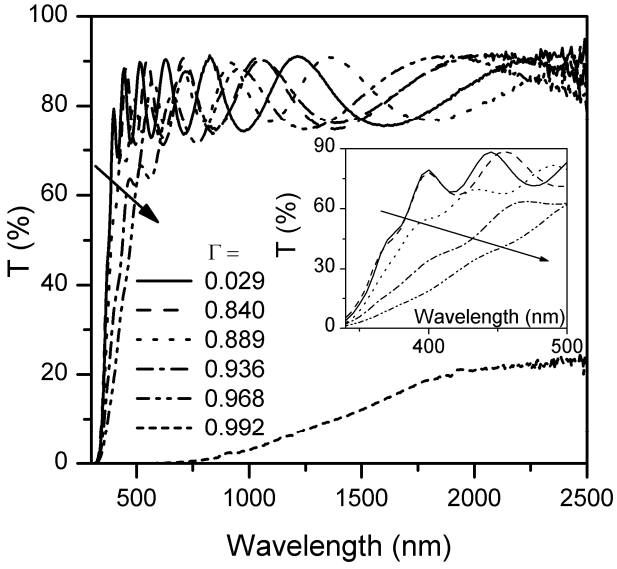
100
80
60
40
20
0
T (%)
500
1000
1500
2000
2500
Wavelength (nm)
Γ =
0.029
0.840
0.889
0.936
0.968
0.992
90
60
30
0
T (%)
400
500
Wavelength (nm)

Fig. 7

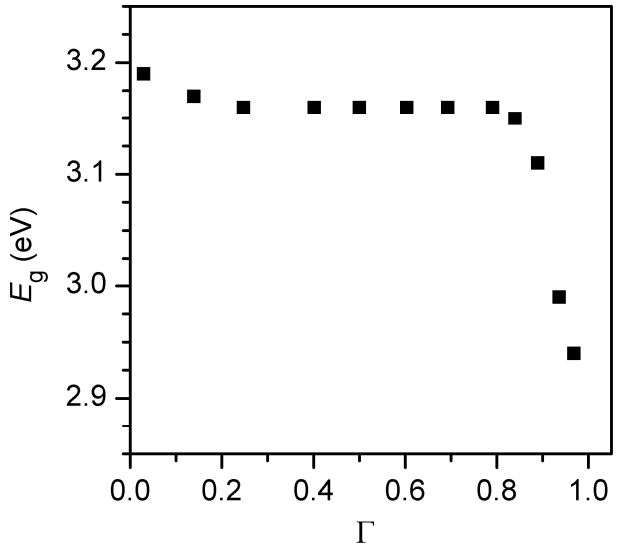

Fig. 8